Investigating Lattice Strain Impact on the Alloyed Surface of Small Au@PdPt Core-Shell Nanoparticles

Journal:	*Nanoscale*
Manuscript ID	NR-COM-02-2020-001021.R1
Article Type:	Communication
Date Submitted by the Author:	20-Mar-2020
Complete List of Authors:	Williams, Benjamin; Boston College, Chemistry Yaguchi, Momo; Boston College, Chemistry Lo, Wei-Shang; Boston College, Chemistry Kao, Chen-Rui; Academia Sinica, Institute of Chemistry Lamontagne, Leo; Boston College, Chemistry Sneed, Brian; Boston College, Chemsitry Brodsky, Casey; Harvard University, Chemistry and Chemical Biology Chou, Lien-Yang; Boston College, Chemistry Kuo, Chun-Hong; Academia Sinica, Institute of Chemistry; National Central University, Institute of Materials Science and Engineering Tsung, Chia-Kuang; Boston College, Chemistry

Investigating Lattice Strain Impact on the Alloyed Surface of Small Au@PdPt Core-Shell Nanoparticles

Benjamin P. Williams†, Momo Yaguchi†, Wei-Shang Lo, Chen-Rui Kao#, Leo K. Lamontagne, Brian T. Sneed, Casey N. Brodsky, Lien-Yang Chou, Chun-Hong Kuo#,*, and Chia-Kuang Tsung*

Department of Chemistry, Merkert Chemistry Center, Boston College, 2609 Beacon Street, Chestnut Hill, Massachusetts 02467, United States.

#Institute of Chemistry, Academia Sinica, No. 128, Section 2, Academia Rd, Nangang District, Taipei City, Taiwan 115.

†These authors contributed equally to this work.

KEYWORDS: *Au, Pd, Pt, alloy, core-shell, octahedra, lattice strain, electrocatalysis, formic acid oxidation, nanoparticles*

ABSTRACT: We investigated lattice strain on alloyed surfaces using ~10 nm core-shell nanoparticles with controlled size, shape, and composition. We developed a wet-chemistry method for synthesizing small octahedral PdPt alloy nanoparticles and Au@PdPt core-shell nanoparticles with Pd-Pt alloy shells and Au cores. Upon introduction of the Au core, the size and shape of the overall nanostructure and the composition of the alloyed PdPt were maintained, enabling the use of the electrooxidation of formic acid as a probe to compare the surface structures with different lattice strain. We have found that the structure of the alloyed surface is indeed impacted by the lattice strain generated by the Au core. To further reveal the impact of lattice strain, we fine-tuned the shell thickness. Then, we used synchrotron-based x-ray diffraction to investigate the degree of lattice strain and compared the observations with the results of the formic acid electrooxidation, suggesting that there is an optimal intermediate shell thickness for high catalytic activity.

INTRODUCTION

Precious metal nanoparticles are the major active catalyst in many electrochemical energy conversion processes.[1-5] Due to their high cost, much effort has been given to the ongoing improvement of their catalytic properties by refining their shape[6-12] and alloying them with other metals.[13-16] During this process, the influence of shape and alloying effects on catalytic activity has been studied.[3, 17-19] Even the investigation of the combined effect of shape and alloying has been reported: Markovic[20] has shown for Pt_3Ni crystal facets, for example, that alloying nickel into platinum can increase activity toward oxygen reduction, with a dependence on shape related to the dominant facet. This change in activity can be explained by an energy shift in the d-band center that affects catalysis by increasing or decreasing reactant absorption energies, leading to higher activities.[21-23] Creating surface lattice strain, which can similarly shift the d-band center, has been reported to promote catalytic activity as well.[1, 13, 24-29] However, unlike alloying and shape control, which must be located at the surface to impact catalytic activity, lattice strain can impact surface reactivity through metal-metal interfaces that are more than a few atomic layers away.[1] This extended range of impact allows lattice strain to be imparted to a shape- and composition-controlled system where its effect can be tested without changing the dominant surface facet or composition.

To test this hypothesis, we selected a simple model system, choosing an octahedral shape, Pd-Pt alloy composition, and a Au core as the lattice strain source. There is an approximately 5% lattice mismatch between the Au core and PdPt shell that provides the lattice strain. The nanoparticles were characterized using transmission electron microscopy (TEM) and energy dispersive X-ray spectroscopy (EDS). The composition of the nanoparticles was characterized through scanning-TEM/EDS (STEM/EDS). The formic acid oxidation reaction (FOR) is used as a probe reaction to investigate the surface because it has been demonstrated to be sensitive to surface electronic structure.[30, 31] We synthesized ~10 nm PdPt alloyed nanooctahedra and ~10 nm core-alloyed shell nanooctahedra with an 8 nm Au octahedral core and a 2 nm PdPt alloyed shell. Three alloy compositions were tested, Pd_3Pt_1, Pd_1Pt_1, and Pd_1Pt_3. It was found that the lattice strain generated by the Au core indeed changed FOR activity, regardless of the alloy composition. Core-alloyed shell nanoparticles were further synthesized with the same core size but different shell thickness (while maintaining shape and alloy composition).[32, 33] Their FOR performance was compared with lattice strain analyzed by synchrotron-based high resolution powder x-ray diffraction (HRXRD). It was observed that there is an optimal intermediate level of lattice strain that maximizes FOR performance.

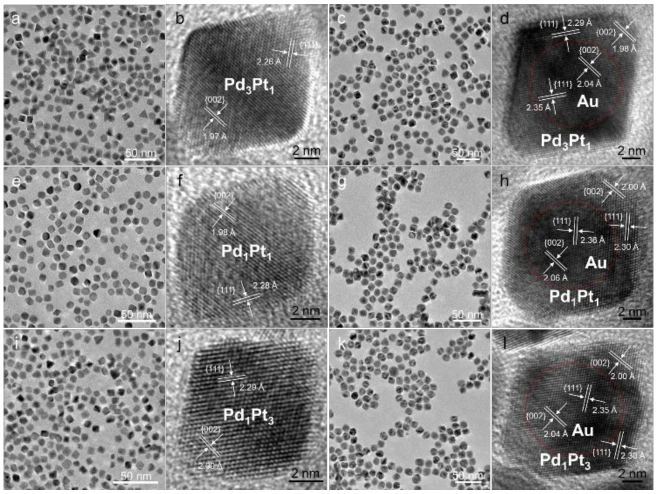

Figure 1. TEM images of a, e, i) PdPt alloy octahedral nanoparticles and c, g, k) Au@PdPt core-shell octahedral nanoparticles. High-resolution TEM images show the clear lattice fringes of b, f, j) PdPt and d, h, l) Au@PdPt with different Pd/Pt compositions. The dashed red line surrounds the Au core, in which lattice spacings are larger than in the shell due to the larger lattice parameter of Au than Pd and Pt (a_{Au} 4.087 Å, a_{Pd} 3.867 Å, and a_{Pt} 3.920 Å, respectively).

RESULTS AND DISCUSSION

To have small nanoparticles with well-defined size, shape, alloying, and core-shell structure is not straightforward. We adapted a hydrothermal synthesis mediated by two common strategies: co-reduction[34] and seed-mediated growth.[35] The octahedral alloyed nanoparticles were synthesized through the hydrothermal co-reduction[34] of Pd^{2+} and Pt^{2+} by sodium citrate at 110 °C. Cetyltrimethylammonium bromide (CTAB) was used as a capping agent. The weak reducing agent and mild reaction temperature slow reduction and deposition rates, promoting formation of the {111} facets that dominate the surface of the octahedral shape. We found that the amount of oxygen in the synthesis solution is critical since oxygen could etch newborn nuclei and slow the growth rate. If too much oxygen is introduced, it leads to octahedra and nanoprisms that are still dominated by {111} facets but larger than our target size (Figure S1). Adjusting the molar ratio between the reactant Pt^{2+} and Pd^{2+} ions allowed for the three different compositions of the Pd_3Pt_1, Pd_1Pt_1, and Pd_1Pt_3 octahedra (Figures 1, S2, and S3). To make core-shell structures, we synthesized 8 nm Au seeds of single crystalline structure and monodisperse truncated octahedral shape (Figure S4). They are then added to the growth solution of Pd and Pt (DI water, Pt^{2+}, Pd^{2+}, and sodium citrate) before reduction in the oven. After reaction, Au@PdPt core-alloyed shell octahedra formed (Figures 1, S2, and S3).

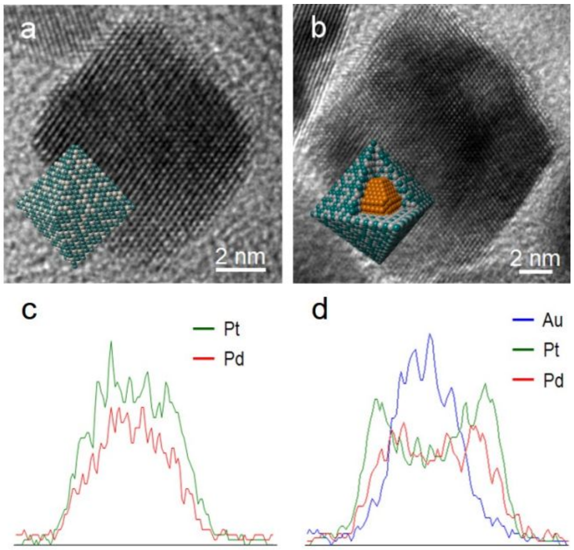

Figure 2. TEM images and TEM-EDS line-scanning analysis on (a,c) an octahedral Pd_1Pt_3 alloy and (b,d) Au@Pd_1Pt_3 core-shell octahedral nanoparticles.

TEM images in Figure 1 show uniform PdPt alloy and Au@PdPt core-shell octahedral nanoparticles with three compositions. Figure 1b, 1f, and 1j are high-resolution TEM images showing the lattices from the [110] zone axis (octahedra sitting on a (110) edge). The HRTEM images show that all the nanoparticles are single crystalline with {111} facets exposed on their alloyed surface. HRTEM images of core-shell nanoparticles display the lattices of both the Au cores and the PdPt alloy shells (Figures 1d, 1h, and 1l). The PdPt shells are conformal, single crystalline alloys, and epitaxial to the Au cores. A slight expansion of the shell lattice can be seen due to the Au core. Energy dispersive x-ray spectroscopy (EDS) was carried out to investigate the elemental distribution in the nanoparticles (Figure 2). Pd to Pt ratios of alloy nanoparticles and alloy shells are controlled to be similar (Tables S1 and S2).

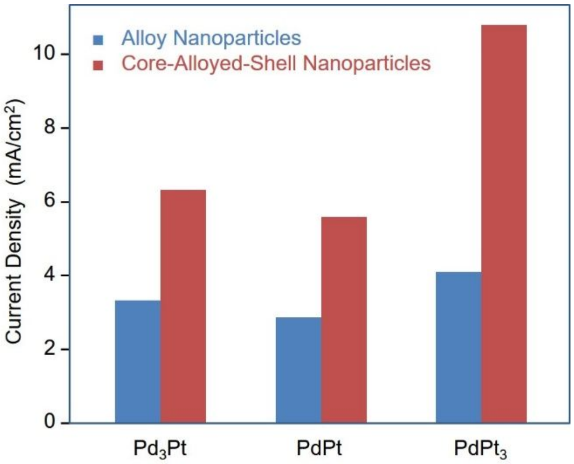

Figure 3. Current density of FOR on PdPt alloy and Au@PdPt core-alloyed shell octahedral nanoparticles with different Pd:Pt ratios but similar thicknesses.

Formic acid is a good choice for chemical fuel cells due to its high energy density (1740 Wh/kg) and ease of storage.[36] It is generally accepted that there are possible direct and indirect FOR pathways.[37-39] In the direct pathway, the removal of hydrogen happens either from the C-H bond or the O-H bond of HCOOH, followed by oxidation on the catalyst surface to generate CO_2. The indirect pathway is known as the non-Faradaic (i.e. without electron flow) dehydrogenation of formic acid, in which activated CO_{ads} is produced first and then further oxidized to form CO_2. It was found that the current density of both pathways is highly dependent on the metal surface structure; therefore, FOR is a sensitive probe to test the surface of Pt-based nanoparticles.[38-40] Polarization curves indicate that the FOR on our alloy and core-shell nanoparticles follows the indirect pathway (Figure S5). In the cathodic scan, the peak between 0.6 V and 0.0 V comes from the oxidation of CO_{ads} and Figure 3 summarizes the cathodic scan current densities of alloy and core-shell nanoparticles. It shows that alloying has altered the activity;[20] however, the influence of the Au core is more significant as all the core-shell nanoparticles have higher current density than their alloy counterparts. This result suggests that the Au core has a large impact on the alloy surface, which we believe originates from lattice strain caused by lattice mismatch between the Au core and PdPt shell. Differences in activity between the core-shell structures are attributed to differences in composition, as they follow a similar trend to that seen for the pure PdPt nanostructures. It should be noted that there could be slight differences in lattice strain among the core-shell structures due to the variation in composition, but these should be slight due to the similar lattice constants of Pd and Pt and thicknesses of the alloy shells.

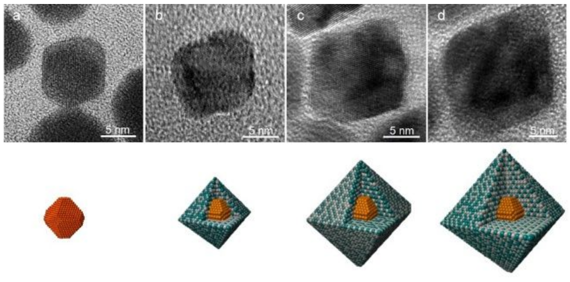

Figure 4. TEM images showing a) Au cores and PdPt shells of different thicknesses, b) 1.3 nm, c) 2.3 nm, and d) 3.5 nm.

To further investigate the effect of lattice strain on the alloy surface, we have tuned the strain by preparing $Au@Pd_1Pt_3$ nanoparticles with thinner and thicker shells (see experimental section). Three $Au@Pd_1Pt_3$ core-shell samples of shell thicknesses of 1.3 nm, 2.3 nm, and 3.5 nm (Figure S4f-S4h) show a Pd to Pt ratio of 1.0:2.9, 1.0:2.5, and 1.0:2.5, respectively (Table S3). Shell thicknesses are calculated based on the initial size of the Au core and the final size of the Au-PdPt core-shell nanoparticle. EDS line scanning was also performed and agrees well with the assigned thicknesses. Figure S6 shows that these nanoparticles have an octahedral shape regardless of shell thickness. To estimate lattice strain, synchrotron-based x-ray diffraction (XRD) with an x-ray wavelength of 1.0332 Å was performed. For comparison, we also included the Pd_1Pt_3 alloy nanoparticles. Figure 5 includes the (220) peaks of the XRD patterns of Pd_1Pt_3 alloy and $Au@Pd_1Pt_3$ core-shell nanoparticles within the range from 41° to 45°. In this range, there are two peaks for $Au@Pd_1Pt_3$ core-shell nanoparticles but only one for Pd_1Pt_3 alloy nanoparticles. Peaks located around 42° are attributed to the Au cores (Figure S7) and peaks located between 43° and 44° correspond to the Pd_1Pt_3 alloy shells. There is a clear trend of peaks shifting from 43.49° to 43.98° for the samples with different thicknesses. This shift indicates that the 220 d-spacing of the alloy exhibits a lattice expansion from 0.1380 nm to 0.1394 nm with decreasing thickness. Using these lattice parameters (Table S4), we estimated lattice strain (δ_s). $a°_{PdPt}$ is the estimated lattice parameter of the alloy obtained from Vegard's law, in which the lattice parameter $a°_{AB}$ of a homogeneous alloy A_xB_{1-x} is the sum of $xa°_A$ and $(1-x)a°_B$. a_{PdPt} is the experimental value of the lattice parameter. Lattice strain, δ_s, is obtained by comparing the difference between $a°_{PdPt}$ and a_{PdPt}, representing the variation in surface atomic arrangement due to the strain force. For $Au@Pd_1Pt_3$, the thinner the shell, the larger the lattice strain. The estimated number of Pd_1Pt_3 atomic layers in the $Au@Pd_1Pt_3$ samples is about 5 (t = 1.3 nm), 10 (t = 2.3 nm), and 15 (t = 3.5 nm). Fewer atomic layers in the shell allow for more surface influence from lattice mismatch at the interface of Au core and alloy shell. Strain shrinks as atomic layers increase because the surface becomes farther and farther away from the source of the lattice mismatch. It should be noted that changes in overall particle size can also effect surface lattice strain; however, this effect is normally strong in small (<3 nm) nanoparticles.[41] Over the size range studied here, these effects should be negligible compared to strain induced by the Au core.[42]

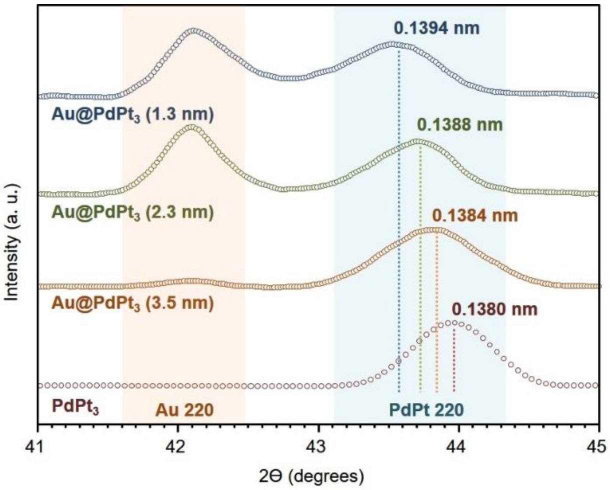

Figure 5. Synchrotron-based XRD patterns of the (220) peaks of Pd_1Pt_3 alloy and $Au@Pd_1Pt_3$ core-alloyed shell nanoparticles with three different shell thickness. The wavelength of the synchrotron x-ray incident on the samples is 1.0332 Å. The broad peaks between 43° and 44°

represent the (220) peak of the Pd_1Pt_3 alloy (shell), which shifts to the left as shell thickness decreases.

These core-alloyed shell nanoparticles were then tested for the FOR. Figure S6 shows CVs of formic acid oxidation on Au@Pd_1Pt_3 nanoparticles with various shell thicknesses. For comparison, we also include pure Pd_1Pt_3 alloyed nanoparticles (Figure 6). In all cases, the Au core increases the current density of the cathodic scans; however, the increase from Pd_1Pt_3 to Au@Pd_1Pt_3 with a thick, 3.5 nm shell is negligible, rising only from 4.09 to 4.11 mA/cm^2. When that thickness is reduced to 2.3 nm, on the other hand, a large jump in current density, to 10.08 mA/cm^2, is seen. As mentioned earlier, we attribute this upturn to the effect of increased lattice strain on the surface that raises the d-band center. For the thin, 1.3 nm shell, though, the current density is decreased back to 5.65 mA/cm^2. We note that this need for optimized structure has been observed in many catalysis studies and indicates that the alloy surface is indeed sensitive to the fine structure of the nanoparticles. There are two potential reasons for this relationship. One possible reason is that when strain is too high, as in the case of the thin shell, the surface lattice strain is relaxed by the formation of surface defects, sapping its catalytic activity. Another explanation could be the influence of the ligand effect. The ligand effect is mainly caused by charge transfer as electron density is transferred from a metal with a higher Fermi level to a metal with a lower Fermi level.[43] This increased filling results in a lowering of the shell's d-band center and a decrease in FOR activity. Lattice strain imparted by Au, on the other hand, raises the d-band center, increasing FOR activity. In the thinnest shell's case, the ligand effect is strong, and charge transfers from the core to the shell, increasing the shell's d-band filling and offsetting the strain effect. When the Pd_1Pt_3 shell becomes sufficiently thick (*t* = 2.3 nm), the strain effect dominates over the ligand effect, resulting in high activity. When the shell is very thick (*t* = 3.5 nm), neither effect is strong and the particles show similar activity to the bimetallic alloy Pd_1Pt_3 with no core.

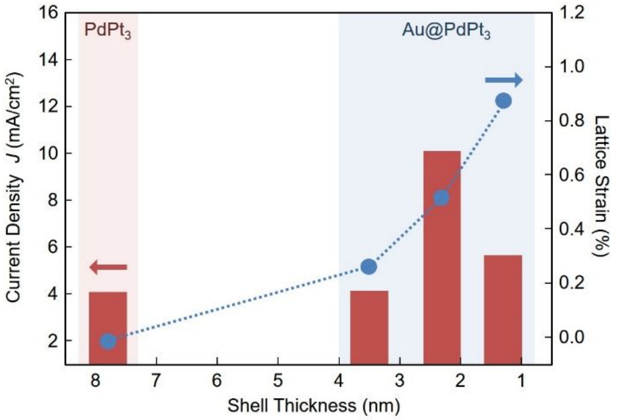

Figure 6. The relation of lattice strain, current density, and thickness of Pd_1Pt_3 alloy domains.

CONCLUSION

In conclusion, to study the lattice strain effect on the alloyed nanoparticle surface, we have synthesized well-controlled Pd_xPt_y alloyed octahedral nanoparticles and Au@Pd_1Pt_3 core-alloyed shell nanoparticles of ~10 nm. We have investigated the surfaces via using FOR as a probe. We have found that the Au core impacts the alloy surface regardless of alloy composition. We have then changed the thickness of the alloy shell to tune the lattice strain and used synchrotron-based XRD to quantify strain. We have compared the surfaces of nanoparticles with different levels of lattice strain that optimizing fine structure is an important consideration when designing nanocatalysts.

METHODS

Chemicals. Palladium (II) chloride ($PdCl_2$, 99 %, Sigma Aldrich), potassium tetrachloroplatinate (II) (K_2PtCl_4, ≧99 %, Sigma Aldrich), gold (III) chloride hydrate ($HAuCl_4$, 99.99%, Sigma Aldrich), cetyltrimethylammonium bromide (CTAB, 98 %, CALBIOCHEM), cetyltrimethylammonium chloride (CTAC, 95 %, TGI), sodium citrate tribasic dehydrate ($C_6H_5Na_3O_7 \cdot 2H_2O$, Sigma Aldrich, 99.5 %) were all used without further purification. Ultrapure distilled and deionized water (18.2 MΩ) was used for all solution preparations. Ultrapure Argon (Ar, Airgas) and carbon monoxide (CO, Airgas) were used during the synthesis.

Synthesis of palladium-platinum alloy octahedral nanoparticles. Octahedral Pd-Pt alloy nanoparticles were prepared by a one-pot hydrothermal method in aqueous solution. A pressure vessel containing 28.988 mL of deionized water, 123.75 mg CTAB was sonicated until the mixture became transparent, indicating the surfactant was completely dissolved. Then, 0.375 mL of 0.01 M H_2PdCl_4 solution (3.75×10^{-3} mmol) and 0.375 mL of 0.01 M K_2PtCl_4 solution (3.75×10^{-3} mmol) were added. The total molar number of Pd^{2+} and Pt^{2+} ions are 7.5×10^{-3} mmol. After bubbling with Ar for 30 minutes, 0.142 mL of 0.1 M sodium citrate solution was added into the resulting salmon-pink-colored solution. The pressure vessel was then placed and heated at 110 °C for 22 hours in the oven. The resulting light-brown-colored solution (Figure S1) was cooled down to room temperature and the products were collected by centrifugation at 12,000 rpm three times. To adjust composition of PdPt alloy, the molar ratio of H_2PdCl_4/K_2PtCl_4 was changed to 1/3 and 3/1 but the total molar number of Pd^{2+} and Pt^{2+} ions were kept the same (7.5×10^{-3} mmol).

Preparation of gold seeds. Spherical gold seeds (sub-10 nm) were prepared by a one-pot hydrothermal method in the aqueous phase. First, 270 mg CTAB was dissolved in 48.513 mL of deionized water. Then, 1.25 mL of 0.01 M $HAuCl_4$ and 0.237 mL of 0.1 M sodium citrate were added into the clear transparent solution, followed by bubbling carbon monoxide for half an hour. We specifically introduce carbon monoxide into the seed synthesis to promote development of the {111} surface. While the nanoparticles do not serve as shape-directing agents, the presence of many {111} surface facets in the seeds promotes epitaxial growth. The bright-orange solution in a pressure vessel was heated at 110 °C for 22 hours and a red-violet-colored solution was obtained.

Synthesis of Au@PdPt core-shell nanooctahedra. In a typical synthesis of octahedral Au@PdPt core-shell nanoparticles, a pressure vessel containing 25.988 mL of deionized water, 123.75 mg CTAB was sonicated until it became transparent. Once the surfactant was dissolved, 3.0 mL of Au-seed solution (7.5×10^{-4} mmol of Au atoms) was added, followed by the further addition of 0.375 mL of 0.01 M H_2PdCl_4 solution and 0.375 mL of 0.01 M K_2PtCl_4 solution. After bubbling with Ar for half an hour, 0.142 mL of 0.1M sodium citrate solution was added into the resulting pale-violet color cloudy solution. The vessel was then heated at 110 °C for 22 hours in the oven. The resulting brown-colored solution (Figure S1) in a pressure vessel was cooled down to room temperature and the products were collected via centrifugation at 12,000 rpm for redispersion in water, where this rinsing was then repeated for a total of three cycles. To make Au@Pd_1Pt_3 nanoparticles of which shell thickness is 2.6, 4.6, and 7.0 nm, total molar number of 1.5×10^{-3}, 7.5×10^{-3}, and 1.125×10^{-2} mmol of H_2PdCl_4 and K_2PtCl_4 were used in a constant Pd^{2+}/Pt^{2+} ratio equal to 1/3.

Sample Preparation. In preparing TEM samples, the synthesized nanoparticles were concentrated into 0.5 mL solution. The solution color was dark brown. Taking one TEM grid (TED PELLA, INC. Lacey Carbon Type-A) with tweezers (Electron Microscopy Sciences Dumoxel - Tweezers), 5 μL sample solution was dropped onto the grid center and left to dry. For the EDS measurement, the same TEM sample grids were used. For synchrotron-based XRD measurements, the sample solution containing nanoparticles was concentrated into around 0.1 mL. The colloid was thick and brownish-black in color. Silicon wafers were used as substrates for SEM and 20 μL of the sample solution dropped onto these and left for drying.

Electrochemical Measurements. A three-electrode cell system was utilized to measure the electrochemical properties. A glassy carbon electrode was used as the working electrode and first polished with 0.3 micron micropolish powder (CH Instruments, Inc.). A saturated calomel electrode (SCE) and a platinum wire were used as a reference and counter electrode, respectively. First, blank scans were performed in N_2-saturated fresh 0.5 M H_2SO_4 solution with the potential scanned in the range from -0.2 V to 1.0 V in order to clean the surface of the working electrode with catalyst. In a typical measurement, the blank scan without catalyst was continued through around 10-20 cycles. Then, the working electrode was taken out from the solution and dried. Next, 5μL of deionized water dispersion of purified nanoparticles was deposited on a glassy carbon electrode. The blank scan was carried out again to clean the surface of sample-deposited working electrode with the same scanning condition for around 200 cycles. For the electro-oxidation of formic acid, the cyclic voltammogram was recorded at a sweep rate of 100 mV/s in N_2-saturated fresh 1 M H_2SO_4 + 1 M formic acid with the potential range from -0.2 V to 1.0 V. The current is normalized by the electrochemically active surface area (ECSA) of catalysts in the electrode, which was estimated from the integrated reduction charge of surface palladium oxide by assuming a charge of 0.42 mC/cm^2 for the reduction of palladium oxide monolayer. For the CO stripping voltammetry measurements, CO gas was bubbled for 30 minutes through 0.1 M $HClO_4$ solution in which the electrode immersed. The electrode was moved to a fresh N_2-saturated 0.1 M $HClO_4$ solution and the CO stripping voltammetry was recorded at a sweep rate of 10 mV/s with the potential range from 0.2 V to 1.2 V.

Instrumentation. Scanning electron microscopy (SEM) images of the samples were obtained using a JEOL JSM 6340F electron microscope. Transmission electron microscopy (TEM) including high-resolution transmission electron microscope (HRTEM) and energy-dispersive X-ray spectroscopy (EDS) studies were performed on a JEOL JEM 2010F electron microscope operating at 200 keV. X-ray of 1.0332 Å from synchrotron radiation monochromatized by Si(111) crystal was used for diffraction. The growth solution was heated using a Thermo Scientific Lindberg Blue M oven. The particles were collected by using Thermo Scientific Sorvall Legend X1R Centrifuge and Eppendorf Centrifuge 5424.

ASSOCIATED CONTENT

Supporting Information. Photographs of alloy and core-shell solutions, TEM images and histogram of Au seeds, TEM images of Pd_1Pt_1 nanoparticles made with oxygen gas, histograms, table of EDS-analyzed elemental composition, polarization curves of formic acid oxidation for alloy and core-shell nanoparticles, TEM images, table of EDS-analyzed elemental composition, polarization curves of formic acid oxidation for Au@Pd_1Pt_3 core-shell nanoparticles with different shell thickness. This information is available free of charge via the internet at http://pubs.acs.org.

AUTHOR INFORMATION

Corresponding Author

*Email: (C.K.T.) frank.tsung@bc.edu

ACKNOWLEDGEMENT

We were partially supported by NSF Grant CHE-1566445. We thank Dr. Zhi Lui and Dr. Martin Kunz for their kind help in Advanced Light Source (ALS) of Lawrence Berkeley National Lab. We also appreciate Dr. Shaul Aloni in The Molecular Foundry of Lawrence Berkeley National Lab for his efforts on STEM elemental analysis. The research is funded by Boston College. C.H.K. appreciates the financial support from the Ministry of Science and Technology, Taiwan (MOST 108-2628-M-001-005-MY3), and Academia Sinica, Taiwan (Innovative Materials and Analytical Techniques Project AS-iMATE-109-22, Sustainability Science Research Project AS-SS-108-02).

REFERENCES

1. P. Strasser, S. Koh, T. Anniyev, J. Greeley, K. More, C.

F. Yu, Z. C. Liu, S. Kaya, D. Nordlund, H. Ogasawara, M. F. Toney and A. Nilsson, *Nat. Chem.*, 2010, **2**, 454-460.

2. M. K. Debe, *Nature*, 2012, **486**, 43-51.
3. R. Narayanan and M. A. El-Sayed, *Nano Lett.*, 2004, **4**, 1343-1348.
4. M. Shao, Q. Chang, J.-P. Dodelet and R. Chenitz, *Chem. Rev.*, 2016, **116**, 3594.
5. S. Sui, X. Wang, X. Zhou, Y. Su, S. Riffat and C.-J. Liu, *J. Mater. Chem. A*, 2017, **5**, 1808.
6. V. Grozovski, J. Solla-Gullon, V. Climent, E. Herrero and J. M. Feliu, *J. Phys. Chem. C*, 2010, **114**, 13802-13812.
7. M. H. Huang and P. H. Lin, *Adv. Funct. Mater.*, 2012, **22**, 14-24.
8. C. Y. Chiu, P. J. Chung, K. U. Lao, C. W. Liao and M. H. Huang, *J. Phys. Chem. C*, 2012, **116**, 23757-23763.
9. Y. H. Chen, H. H. Hung and M. H. Huang, *J. Am. Chem. Soc.*, 2009, **131**, 9114-9121.
10. M. Laskar and S. E. Skrabalak, *ACS Catal.*, 2014, **4**, 1120-1128.
11. M. H. Huang, S. Rej and S.-C. Hsu, *Chem. Commun.*, 2014, **50**, 1634.
12. L. Liu and A. Corma, *Chem. Rev.*, 2018, **118**, 4981.
13. C. G. Cui, L; Li, H; Yu, S; Heggen, M; Strasser, P, *Nano Lett.*, 2012, **12**, 5885-5889.
14. S.-I. Choi, S. Xie, M. Shao, J. H. Odell, N. Lu, H.-C. Peng, L. Protsailo, S. Guerrero, J. Park, X. Xia, J. Wang, M. J. Kim and Y. Xia, *Nano Lett.*, 2013, **13**, 3420-3425.
15. N. Zhang, L. Bu, S. Guo, J. Guo and X. Huang, *Nano Lett.*, 2016, **16**, 5037-5043.
16. L. Bu, N. Zhang, S. Guo, X. Zhang, J. Li, J. Yao, T. Wu, G. Lu, J.-Y. Ma, D. Su and X. Huang, *Science*, 2016, **354**, 1410.
17. N. Tian, Z.-Y. Zhou, S.-G. Sun, Y. Ding and Z. L. Wang, *Science*, 2007, **316**, 732-735.
18. P. Du, P. Wu and C. Cai, *J. Phys. Chem. C*, 2015, **119**, 18352.
19. J. Wu, P. Li, Y.-T. F. Pan, S. Warren, X. Yin and H. Yang, *Chem. Soc. Rev.*, 2012, **41**, 8066-8074.
20. V. R. Stamenkovic, B. Fowler, B. S. Mun, G. F. Wang, P. N. Ross, C. A. Lucas and N. M. Markovic, *Science*, 2007, **315**, 493-497.
21. K. Tedsree, T. Li, S. Jones, C. W. A. Chan, K. M. K. Yu, P. A. J. Bagot, E. A. Marquis, G. D. W. Smith and S. C. E. Tsang, *Nat. Nanotechnol.*, 2011, **6**, 302-307.
22. V. R. Stamenkovic, B. S. Mun, K. J. J. Mayrhofer, P. N. Ross, N. M. Markovic, J. Rossmeisl, J. Greeley and J. K. Norskov, *Angew. Chem.*, 2006, **45**, 2897.
23. A. Kulkarni, S. Siahrostami, A. Patel and J. K. Norskov, *Chem. Rev.*, 2018, **118**, 2302.
24. J. B. Wu, L. Qi, H. J. You, A. Gross, J. Li and H. Yang, *J. Am. Chem. Soc.*, 2012, **134**, 11880-11883.
25. J. H. Yang, J. Yang and J. Y. Ying, *ACS Nano*, 2012, **6**, 9373-9382.
26. M. Luo and S. Guo, *Nat. Rev. Mater.*, 2017, **2**, 17059.
27. T. Nilsson Pingel, M. Joergensen, A. B. Yankovich, H. Groenbeck and E. Olsson, *Nat. Commun.*, 2018, **9**, 1.
28. X. Zhao, S. Chen, Z. Fang, J. Ding, W. Sang, Y. Wang, J. Zhao, Z. Peng and J. Zeng, *J. Am. Chem. Soc.*, 2015, **137**, 2804-2807.
29. C. Cui, L. Gan, M. Heggen, S. Rudi and P. Strasser, *Nat. Mater.*, 2013, **12**, 765-771.
30. V. Mazumder, M. Chi, M. N. Mankin, Y. Liu, O. Metin, D. Sun, K. L. More and S. Sun, *Nano Lett.*, 2012, **12**, 1102-1106.
31. S. Hu, F. Che, B. Khorasani, M. Jeon, C. W. Yoon, J.-S. McEwen, L. Scudiero and S. Ha, *Appl. Catal. B: Environ.*, 2019, **254**, 685-692.
32. D. Wang and Y. Li, *Adv. Mater.*, 2011, **23**, 1044-1060.
33. K. D. Gilroy, A. Ruditskiy, H.-C. Peng, D. Qin and Y. Xia, *Chem. Rev.*, 2016, **116**, 10414.
34. L. Kuai, X. Yu, S. Wang, Y. Sang and B. Geng, *Langmuir*, 2012, **28**, 7168-7173.
35. J. Li, Y. Zheng, J. Zeng and Y. Xia, *Chem.: Eur. J.*, 2012, **18**, 8150-8156.
36. M. T. M. Koper, *Nanoscale*, 2011, **3**, 2054-2073.
37. S. B. Brummer and A. C. Makrides, *J. Phys. Chem.*, 1964, **68**, 1448-&.
38. Y. J. Kang, L. Qi, M. Li, R. E. Diaz, D. Su, R. R. Adzic, E. Stach, J. Li and C. B. Murray, *ACS Nano*, 2012, **6**, 2818-2825.
39. R. Chetty and K. Scott, *J. New Mat. Elect. Syst.*, 2007, **10**, 135-142.
40. H. Zhang, M. Jin and Y. Xia, *Chem. Soc. Rev.*, 2012, **41**, 8035-8049.
41. W. An and P. Liu, *J. Phys. Chem. C*, 2013, **117**, 16144-16149.
42. G. Ouyang, W. G. Zhu, C. Q. Sun, Z. M. Zhu and S. Z. Liao, *Phys. Chem. Chem. Phys.*, 2010, **12**, 1543-1549.
43. W. Tang and G. Henkelman, *J. Chem. Phys.*, 2009, **130**.

TOC graphic

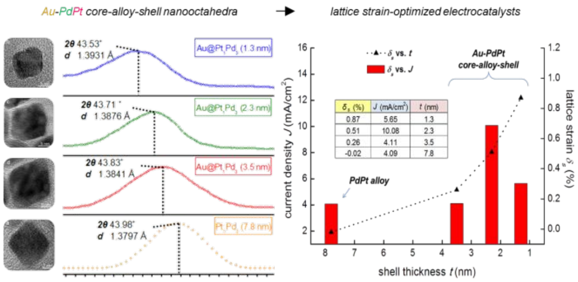

δ_s (%)	J (mA/cm^2)	t (nm)
0.87	5.65	1.3
0.51	10.08	2.3
0.26	4.11	3.5
-0.02	4.09	7.8